

See discussions, stats, and author profiles for this publication at: <https://www.researchgate.net/publication/5671569>

# Hygroscopic Behavior of Substrate-Deposited Particles Studied by micro-FT-IR Spectroscopy and Complementary Methods of Particle Analysis

ARTICLE in ANALYTICAL CHEMISTRY · MARCH 2008

Impact Factor: 5.64 · DOI: 10.1021/ac701638r · Source: PubMed

CITATIONS

64

READS

80

6 AUTHORS, INCLUDING:



**Y. Desyaterik**

Colorado State University

33 PUBLICATIONS 522 CITATIONS

SEE PROFILE



**Paul Gassman**

Pacific Northwest National Laboratory

43 PUBLICATIONS 1,888 CITATIONS

SEE PROFILE



**Hai Wang**

Stanford University

163 PUBLICATIONS 6,410 CITATIONS

SEE PROFILE



**Alexander Laskin**

Pacific Northwest National Laboratory

177 PUBLICATIONS 4,651 CITATIONS

SEE PROFILE

# Hygroscopic Behavior of Substrate-Deposited Particles Studied by micro-FT-IR Spectroscopy and Complementary Methods of Particle Analysis

Yong Liu,<sup>†</sup> Zhiwei Yang,<sup>‡,||</sup> Yuri Desyaterik,<sup>†</sup> Paul L. Gassman,<sup>†</sup> Hai Wang,<sup>§</sup> and Alexander Laskin<sup>\*,†</sup>

William R. Wiley Environmental Molecular Sciences Laboratory, Pacific Northwest National Laboratory, P.O. Box 999, MSIN K8-88, Richland, Washington 99352, Department of Mechanical Engineering, University of Delaware, Newark, Delaware 19716, and Department of Aerospace and Mechanical Engineering, University of Southern California, Los Angeles, California 90089

The application of microscopic Fourier transform infrared (micro-FT-IR) spectroscopy combined with complementary methods of particle analysis is demonstrated here for investigations of phase transitions and hygroscopic growth of micron-sized particles. The approach utilizes the exposure of substrate-deposited, isolated particles to humidified nitrogen inside a sample cell followed by micro-FT-IR spectroscopy over a selected sample area. Phase transitions of NaCl, sea salt, NaNO<sub>3</sub>, and (NH<sub>4</sub>)<sub>2</sub>SO<sub>4</sub> particles are monitored with this technique to evaluate its utility and applicability for particle hydration studies. The results are found in excellent agreement with literature data in terms of (a) reliable and reproducible detection of deliquescence and efflorescence phase transitions, (b) quantitative measurements of water-to-solute ratios in particles as a function of relative humidity, and (c) changes in the IR spectra resulting from phase transitions and changing relative humidity. Additional methods of particle analysis are employed to complement and assist in the interpretation of particle hygroscopicity data obtained from micro-FT-IR measurements. The analytical approach and the experimental setup presented here are relatively simple, inexpensive, readily available and therefore may be practical for hydration studies of environmental particles collected in both laboratory and field studies.

The extent to which atmospheric particles affect air quality and atmospheric environment depends on their hygroscopic properties. During hydration and dehydration, particles change both in size and phase. These changes can have direct and indirect impacts on the Earth's climate through scattering and absorption of solar radiation, formation of clouds, and precipitation.<sup>1–7</sup> It is

well-known that the chemical reactivity of aerosols is highly dependent on particle phase and size.<sup>8,9</sup> For example, the heterogeneous reactions of nitric acid, a pervasive gas-phase pollutant, with sea salt<sup>10–13</sup> and mineral dust<sup>14–16</sup> aerosols are much faster in aqueous phase than in solid phase. Additionally, it has been shown that the uptake coefficient of nitric acid onto deliquesced NaCl particles follows a characteristic rise-then-fall behavior with respect to particle size and that the peak reactivity occurs at a particle diameter of  $\sim 0.7 \mu\text{m}$ .<sup>11</sup> Therefore, a quantitative understanding of the hygroscopic behavior of aerosols under varying atmospheric conditions is critical toward understanding their impact on climate change, atmospheric chemistry, and environment.

Over the last few decades, the hygroscopic properties of environmental particles have been studied in numerous laboratory, field, and modeling studies. Comprehensive accounts of these studies can be found in recent review articles and book chapters.<sup>17–21</sup> Particles composed of soluble compounds exhibit properties of deliquescence, efflorescence, and hygroscopic growth.

- (3) Charlson, R. J.; Schwartz, S. E.; Hales, J. M.; Cess, R. D.; Coakley, J. A.; Hansen, J. E.; Hofmann, D. J. *Science* **1992**, *255*, 423–430.
- (4) Pandis, S. N.; Wexler, A. S.; Seinfeld, J. H. *J. Phys. Chem.* **1995**, *99*, 9646–9659.
- (5) Piliinis, C.; Pandis, S. N.; Seinfeld, J. H. *J. Geophys. Res., [Atmos.]* **1995**, *100*, 18739–18754.
- (6) Chow, J. C.; Bachmann, J. D.; Wierman, S. S. G.; Mathai, C. V.; Malm, W. C.; White, W. H.; Mueller, P. K.; Kumar, N.; Watson, J. G. *J. Air Waste Manage. Assoc.* **2002**, *52*, 973–999.
- (7) Malm, W. C.; Molenaar, J. V. *J. Air. Pollut. Control Assoc.* **1984**, *34*, 899–904.
- (8) Seinfeld, J. H.; Pandis, S. N. *Atmospheric Chemistry and Physics: from Air Pollution to Climate Change*; Wiley and Sons, Inc.: New York, 1998.
- (9) Finlayson-Pitts, B. J.; Pitts, J. N., Jr. *Chemistry of the Upper and Lower Atmosphere*; Academic Press: San Diego, 2000.
- (10) ten Brink, H. M. *J. Aerosol Sci.* **1998**, *29*, 57–64.
- (11) Liu, Y.; Cain, J. P.; Wang, H.; Laskin, A. *J. Phys. Chem. A* **2007**, *111*, 10026–10043.
- (12) Tolocka, M. P.; Saul, T. D.; Johnston, M. V. *J. Phys. Chem. A* **2004**, *108*, 2659–2665.
- (13) Saul, T. D.; Tolocka, M. P.; Johnston, M. V. *J. Phys. Chem. A* **2006**, *110*, 7614–7620.
- (14) Liu, Y.; Gibson, E. R.; Cain, J. P.; Wang, H.; Grassian, V. H.; Laskin, A. *J. Phys. Chem. A*, **2008**, in press.
- (15) Vlasenko, A.; Sjogren, S.; Weingartner, E.; Stenmiller, K.; Gaggeler, H. W.; Ammann, M. *Atmos. Chem. Phys.* **2006**, *6*, 2147–2160.
- (16) Krueger, B. J.; Grassian, V. H.; Laskin, A.; Cowin, J. P. *Geophys. Res. Lett.* **2003**, *30* Art. No. 1148.
- (17) Martin, S. T. *Chem. Rev.* **2000**, *100*, 3403–3453.

\* To whom correspondence should be addressed. E-mail: Alexander.Laskin@pnl.gov. Phone: 1-509-376-8741. Fax: 1-509-376-6066.

<sup>†</sup> Pacific Northwest National Laboratory.

<sup>‡</sup> University of Delaware.

<sup>§</sup> University of Southern California.

<sup>||</sup> Current address: Department of Mechanical and Aerospace Engineering, Princeton University, Princeton, NJ 08544

(1) Andreae, M. O.; Crutzen, P. J. *Science* **1997**, *276*, 1052–1058.

(2) Baker, M. B. *Science* **1997**, *276*, 1072–1078.

When ambient relative humidity (RH) increases to the point known as the deliquescence relative humidity (DRH), particles undergo a phase transition from solid particles to liquid droplets. With a further increase in RH, the droplets continue to absorb water and undergo hygroscopic growth. During dehydration, the droplets lose water by evaporation with the decrease of RH and become metastable supersaturated solution below DRH. When the RH is low enough, metastable droplets may rapidly shed all their water content and effloresce (crystallize). This phase transition takes place at efflorescence relative humidity (ERH), which is usually lower than the DRH for the same aerosol.<sup>17,21,22</sup> Such hysteresis phenomenon, stemming from the suppression of heterogeneous and homogeneous nucleation,<sup>17,22</sup> is not found in bulk solution but has been extensively observed in aerosols.<sup>19–41</sup> For example, NaCl particles have DRH and ERH at ~75 and ~48%, respectively.<sup>24</sup> DRH, ERH, and hygroscopic growth factors of aerosols are determined by chemical compositions and thermodynamics<sup>17,42</sup> and are also influenced by particle size and morphology.<sup>41,43–46</sup> Quantitative information on

the DRH, ERH, and hygroscopic growth of particles is an important prerequisite for computer modeling of dynamics, transport, heterogeneous chemistry, and radiative effects of environmental aerosols.

A number of experimental approaches have been advanced to study the hygroscopic properties of aerosols. The single particle levitation technique, sometimes assisted with Raman and Mie resonance spectroscopy,<sup>18,22,24,47–56</sup> has been the most commonly used and has provided the vast majority of data on physical and chemical properties of typical aerosols. In the past decade, flow tube techniques have been used to measure hygroscopicity of free streaming particles using Fourier transform infrared (FT-IR) spectroscopy<sup>26–29,57,58</sup> in concert with a humidified tandem differential mobility analyzer (HTDMA).<sup>59–64</sup> Flow systems with RH controlled nephelometer<sup>37</sup> and aerosol hydration spectrometer<sup>65</sup> have also been employed. More recently, optical<sup>33,34,66,67</sup> and environmental electron microscopy<sup>36,68–75</sup> techniques have been applied to monitor the hydration and dehydration of particles mounted on hydrophobic substrates. Each of the above referenced techniques has its own advantages and disadvantages. For

(18) Tang, I. N. In *Aerosol Chemical Processes in the Environment*; Spurny, K. R., Ed.; CRC Press, LLC: Boca Raton, FL, 2000; pp 61–80.  
 (19) Tang, I. N.; Fung, K. H.; Imre, D. G.; Munkelwitz, H. R. *Aerosol. Sci. Technol.* **1995**, *23*, 443–453.  
 (20) Tang, I. N.; Munkelwitz, H. R. *J. Geophys. Res., [Atmos.]* **1994**, *99*, 18801–18808.  
 (21) Tang, I. N.; In *Generation of Aerosols and Facilities for Exposure Experiments*; Willeke, K., Ed.; Ann Arbor Science Publishers, Inc.: Ann Arbor, MI, 1980; pp 153–167.  
 (22) Tang, I. N.; Tridico, A. C.; Fung, K. H. *J. Geophys. Res., [Atmos.]* **1997**, *102*, 23269–23275.  
 (23) Tang, I. N. *J. Aerosol Sci.* **1976**, *7*, 361–371.  
 (24) Tang, I. N. *J. Geophys. Res., [Atmos.]* **1997**, *102*, 1883–1893.  
 (25) Tang, I. N.; Munkelwitz, H. R.; Davis, J. G. *J. Aerosol Sci.* **1978**, *9*, 505–511.  
 (26) Gibson, E. R.; Hudson, P. K.; Grassian, V. H. *J. Phys. Chem. A* **2006**, *110*, 11783–11799.  
 (27) Cziczo, D. J.; Abbatt, J. P. D. *J. Geophys. Res., [Atmos.]* **1999**, *104*, 13781–13790.  
 (28) Cziczo, D. J.; Abbatt, J. P. D. *J. Phys. Chem. A* **2000**, *104*, 2038–2047.  
 (29) Cziczo, D. J.; Nowak, J. B.; Hu, J. H.; Abbatt, J. P. D. *J. Geophys. Res., [Atmos.]* **1997**, *102*, 18843–18850.  
 (30) Han, J. H.; Martin, S. T. *J. Geophys. Res., [Atmos.]* **1999**, *104*, 3543–3553.  
 (31) Fortin, T. J.; Shilling, J. E.; Tolbert, M. A. *J. Geophys. Res., [Atmos.]* **2002**, *107*, Art. No. 4088.  
 (32) Onasch, T. B.; Siefert, R. L.; Brooks, S. D.; Prenni, A. J.; Murray, B.; Wilson, M. A.; Tolbert, M. A. *J. Geophys. Res., [Atmos.]* **1999**, *104*, 21317–21326.  
 (33) Pant, A.; Fok, A.; Parsons, M. T.; Mak, J.; Bertram, A. K. *Geophys. Res. Lett.* **2004**, *31*, Art. No. L12111.  
 (34) Pant, A.; Parsons, M. T.; Bertram, A. K. *J. Phys. Chem. A* **2006**, *110*, 8701–8709.  
 (35) Peng, C. G.; Chan, C. K. *Atmos. Environ.* **2001**, *35*, 1183–1192.  
 (36) Wise, M. E.; Biskos, G.; Martin, S. T.; Russell, L. M.; Buseck, P. R. *Aerosol Sci. Technol.* **2005**, *39*, 845–856.  
 (37) Dougle, P. G.; Veeffkind, J. P.; ten Brink, H. M. *J. Aerosol Sci.* **1998**, *29*, 375–386.  
 (38) Badger, C. L.; George, I.; Griffiths, P. T.; Braban, C. F.; Cox, R. A.; Abbatt, J. P. D. *Atmos. Chem. Phys.* **2006**, *6*, 755–768.  
 (39) Garland, R. M.; Wise, M. E.; Beaver, M. R.; DeWitt, H. L.; Aiken, A. C.; Jimenez, J. L.; Tolbert, M. A. *Atmos. Chem. Phys.* **2005**, *5*, 1951–1961.  
 (40) Xu, Q.; DeWitte, M.; Sloan, J. J. *Atmos. Environ.* **2003**, *37*, 911–919.  
 (41) Gao, Y. G.; Chen, S. B.; Yu, L. E. *J. Phys. Chem. A* **2006**, *110*, 7602–7608.  
 (42) Clegg, S. L.; Brimblecombe, P.; Wexler, A. S. *J. Phys. Chem. A* **1998**, *102*, 2155–2171.  
 (43) Li, X. H.; Wang, F.; Lu, P. D.; Dong, J. L.; Wang, L. Y.; Zhang, Y. H. *J. Phys. Chem. B* **2006**, *110*, 24993–24998.  
 (44) Biskos, G.; Malinowski, A.; Russell, L. M.; Buseck, P. R.; Martin, S. T. *Aerosol Sci. Technol.* **2006**, *40*, 97–106.  
 (45) Biskos, G.; Paulsen, D.; Russell, L. M.; Buseck, P. R.; Martin, S. T. *Atmos. Chem. Phys.* **2006**, *6*, 4633–4642.  
 (46) Biskos, G.; Russell, L. M.; Buseck, P. R.; Martin, S. T. *Geophys. Res. Lett.* **2006**, *33*, Art. No. L07801.

(47) Fung, K. H.; Tang, I. N. In *Aerosol Chemical Processes in the Environment*; Spurny, K. R., Ed.; CRC Press, LLC: Boca Raton, FL, 2000; pp 177–195.  
 (48) Tang, I. N.; Munkelwitz, H. R. *J. Appl. Meteorol.* **1994**, *33*, 791–796.  
 (49) Widmann, J. F.; Aardahl, C. L.; Davis, E. J. *TrAC, Trends Anal. Chem.* **1998**, *17*, 339–345.  
 (50) Davis, E. J. *Aerosol Sci. Technol.* **1997**, *26*, 212–254.  
 (51) Aardahl, C. L.; Vehring, R.; Davis, E. J.; Schweiger, G.; Swanson, B. D. *J. Aerosol Sci.* **1997**, *28*, 1491–1505.  
 (52) Peng, C. G.; Chow, A. H. L.; Chan, C. K. *Pharm. Res.* **2000**, *17*, 1104–1109.  
 (53) Choi, M. Y.; Chan, C. K. *J. Phys. Chem. A* **2005**, *109*, 1042–1048.  
 (54) Choi, M. Y.; Chan, C. K. *Environ. Sci. Technol.* **2002**, *36*, 2422–2428.  
 (55) Chan, C. K.; Kwok, C. S.; Chow, A. H. L. *Pharm. Res.* **1997**, *14*, 1171–1175.  
 (56) Chan, M. N.; Chan, C. K. *Environ. Sci. Technol.* **2003**, *37*, 5109–5115.  
 (57) Schlenker, J. C.; Malinowski, A.; Martin, S. T.; Hung, H. M.; Rudich, Y. J. *Phys. Chem. A* **2004**, *108*, 9375–9383.  
 (58) Schlenker, J. C.; Martin, S. T. *J. Phys. Chem. A* **2005**, *109*, 9980–9985.  
 (59) Cruz, C. N.; Pandis, S. N. *Environ. Sci. Technol.* **2000**, *34*, 4313–4319.  
 (60) Hameri, K.; Laaksonen, A.; Vakeva, M.; Suni, T. *J. Geophys. Res., [Atmos.]* **2001**, *106*, 20749–20757.  
 (61) Hameri, K.; Vakeva, M.; Hansson, H. C.; Laaksonen, A. *J. Geophys. Res., [Atmos.]* **2000**, *105*, 22231–22242.  
 (62) Joutsensaari, J.; Vaattovaara, P.; Vesteninen, M.; Hameri, K.; Laaksonen, A. *Atmos. Chem. Phys.* **2001**, *1*, 51–60.  
 (63) Stanier, C. O.; Khlystov, A. Y.; Chan, W. R.; Mandiro, M.; Pandis, S. N. *Aerosol Sci. Technol.* **2004**, *38*, 215–228.  
 (64) Weingartner, E.; Gysel, M.; Baltensperger, U. *Env. Sci. Technol.* **2002**, *36*, 55–62.  
 (65) Hegg, D. A.; Covert, D. S.; Crahan, K. K.; Jonsson, H. H.; Liu, Y. *Geophys. Res. Lett.* **2006**, *33*, Art. No. L21808.  
 (66) Parsons, M. T.; Knopf, D. A.; Bertram, A. K. *J. Phys. Chem. A* **2004**, *108*, 11600–11608.  
 (67) Parsons, M. T.; Mak, J.; Lipetz, S. R.; Bertram, A. K. *J. Geophys. Res., [Atmos.]* **2004**, *109*, Art. No. D06212.  
 (68) Ebert, M.; Inerle-Hof, M.; Weinbruch, S. *Atmos. Environ.* **2002**, *36*, 5909–5916.  
 (69) Hoffman, R. C.; Laskin, A.; Finlayson-Pitts, B. J. *J. Aerosol Sci.* **2004**, *35*, 869–887.  
 (70) Zuberi, B.; Johnson, K. S.; Aleks, G. K.; Molina, L. T.; Molina, M. J.; Laskin, A. *Geophys. Res. Lett.* **2005**, *32*, Art. No. L01807.  
 (71) Laskin, A.; Cowin, J. P.; Iedema, M. J. *J. Electron Spectrosc. Relat. Phenom.* **2006**, *150*, 260–274.  
 (72) Laskin, A.; Gaspar, D. J.; Wang, W.; Hunt, S. W.; Cowin, J. P.; Colson, S. D.; Finlayson-Pitts, B. J. *Science* **2003**, *301*, 340–344.  
 (73) Semeniuk, T. A.; Wise, M. E.; Martin, S. T.; Russell, L. M.; Buseck, P. R. *J. Atmos. Chem.* **2007**, *56*, 259–273.  
 (74) Wise, M. E.; Semeniuk, T. A.; Bruinjtjes, R.; Martin, S. T.; Russell, L. M.; Buseck, P. R. *J. Geophys. Res., [Atmos.]* **2007**, *112*, Art. No. D10224.  
 (75) Matsumura, T.; Hayashi, M. *Aerosol Sci. Technol.* **2007**, *41*, 770–774.

instance, environmental scanning electron microscopy (ESEM) and environmental transmission electron microscopy (ETEM) enable in-situ, high-resolution, qualitative observation of the morphological changes of individual particles caused by changing RH. However, microscopy methods provide no quantitative information about the water content of hydrating particles. Water contents can be inferred from the levitation and the HTDMA experiments. FT-IR spectroscopy,<sup>26,39,69,76–78</sup> despite an inability to visualize particle morphology, enables the qualitative and often quantitative detection of even minor changes in the particles phase and their water content. For this reason, FT-IR spectroscopy has become an increasingly valuable technique in aerosol studies nowadays. Better sensitivity in the detection of the condensed-phase compounds can be achieved using micro-FT-IR spectroscopy. The technique couples an infrared spectrometer to a visible-light microscope. This approach was recently reported by Bertram and co-workers<sup>79</sup> who successfully recorded the phase transition and hygroscopic growth of a single NaCl particle of approximately 5  $\mu\text{m}$  in diameter mounted on a hydrophobic substrate. A similar approach employing micro-Raman spectroscopy has been used for measurements of the DRH and ERH of 10–100  $\mu\text{m}$   $\text{NaNO}_3$  and  $\text{MgSO}_4$  particles sequestered on a quartz substrate.<sup>43,80</sup>

There are some advantages inherent in the analysis of particles mounted on a substrate. Analysis of a fixed amount of analyte in each series of experiment can simplify quantitative data assessment.<sup>76,81</sup> Complementary analytical techniques may be applied for the analysis of similar or even identical samples.<sup>82–84</sup> Hygroscopic properties of particles can be probed before and after controlled exposures to trace gaseous air pollutants to elucidate the effects of particle aging.<sup>11,14,85</sup> Last, it has the ability to study the hygroscopic properties of field-collected particles.<sup>73,84,86</sup>

In this work, we demonstrate the application of micro-FT-IR technique to study the hygroscopic properties of micron-size particles deposited on filmed electron microscopy grids. Four atmospherically relevant aerosols with known hygroscopic properties<sup>17</sup> were selected for the case studies discussed herein. They are NaCl, sea salt,  $\text{NaNO}_3$ , and  $(\text{NH}_4)_2\text{SO}_4$ . We use the changes in IR spectra, along with the integrated absorbance of the water and the solute-specific bands, to determine DRH, ERH, and

hygroscopic growth factors of particles. We also present results of complementary analyses of particle-on-substrate samples using scanning electron microscopy with energy-dispersed analysis of X-rays (SEM/EDX), time-of-flight secondary ionization mass spectrometry (TOF-SIMS), and X-ray diffraction (XRD) analysis. These techniques augment the interpretation of the particle hygroscopicity data obtained from the micro-FT-IR experiments. We demonstrate that the hygroscopic properties of the particles studied can be quantitatively determined from the underlying micro-FT-IR technique.

## EXPERIMENTAL SECTION

**Materials and Sample Preparation.** Aerosols of NaCl,  $\text{NaNO}_3$ , and  $(\text{NH}_4)_2\text{SO}_4$  were atomized from aqueous 0.5 M solutions prepared from reagent-plus-grade chemicals (99.99+% purity, Aldrich). An aerosol of sea salt was atomized from seawater taken from Sequim Bay (Pacific Ocean), WA. The generated aerosols were dried down to ~30–35% RH in a diffusion drier (TSI, Inc., model 3062) prior to sizing and substrate deposition using a micro-orifice uniform deposit impactor (MOUDI) (MSP, Inc., model 110). For this study, we used the fifth stage of the MOUDI for particle collection. The aerodynamic cutoff size of the fifth stage is 1.0  $\mu\text{m}$ . The particles were deposited on filmed grid substrates (carbon type-B, 400 mesh copper grids, Ted Pella, Inc.) and chips of silicon wafer mounted on the impaction plate of the fifth stage. Identical to previous studies,<sup>11,14,85</sup> the size uniformity of deposited particles was confirmed by computer-controlled scanning electron microscopy (CCSEM). The number size distributions of deposited particles were log-normal with median diameters  $\bar{D} = 1.01 \mu\text{m}$  for NaCl, 0.97  $\mu\text{m}$  for sea salt, 1.03  $\mu\text{m}$  for  $\text{NaNO}_3$ , and 0.77  $\mu\text{m}$  for  $(\text{NH}_4)_2\text{SO}_4$  based on the CCSEM measurements of equivalent circle diameters of projected areas of particles in microscopy images. The geometric standard deviations fall within the range of  $\sigma = 1.3$  to 2.1.

**Fourier Transform Infrared micro-Spectroscopy (micro-FT-IR).** The micro-FT-IR setup and the sample cell are illustrated in Figure 1. The apparatus is comprised of a Bruker A590 IR optical microscope interfaced with a Bruker IFS 66/S FT-IR spectrometer. The microscope is equipped with a liquid nitrogen-cooled mercury–cadmium–telluride (MCT) detector. The IR beam is directed into the microscope by a mirror after leaving the interferometer. In addition, a visible-light source is mounted on the microscope to allow for visual examination and positioning of the sample. Turning mirrors are used to switch between pathways for visible and IR irradiation of the sample. The Cassegrainian optics are used to focus the IR beam on the sample (Cassegrainian condenser) and to collect the transmitted IR light after its interaction with the sample (Cassegrainian objective). An aperture is placed on the optical path after the objective and defines the area of the sample over which the IR spectrum is collected. After the aperture, the IR beam is focused onto the MCT detector.

Micro-FT-IR experiments were performed as follows. First, the microscope was set in the optical mode, which allows only specific circular area of the sample, defined by the aperture, to be probed in each experiment. After switching the microscope to the IR transmission mode, FT-IR absorbance spectra were acquired by co-adding 512 scans at a resolution of 4  $\text{cm}^{-1}$ . Condensed-phase water in the particles is observed from OH stretching at ~3400

- (76) Zhao, L. J.; Zhang, Y. H.; Wang, L. Y.; Hu, Y. A.; Ding, F. *Phys. Chem. Chem. Phys.* **2005**, *7*, 2723–2730.
- (77) Zhao, L. J.; Zhang, Y. H.; Wei, Z. F.; Cheng, H.; Li, X. H. *J. Phys. Chem. A* **2006**, *110*, 951–958.
- (78) Shilling, J. E.; Tolbert, M. A. *J. Phys. Chem. A* **2004**, *108*, 11314–11320.
- (79) Parsons, M. T.; Fok, A.; Mak, J.; Lipetz, S. R.; Pant, A.; Haddrell, A.; Agnes, G. R.; Bertram, A. K. *Eos Trans. AGU*; 2003, 84(16) *Fall Meet. Suppl.*, Abstract A51F-0758.
- (80) Wang, F.; Zhang, Y. H.; Li, S. H.; Wang, L. Y.; Zhao, L. J. *Anal. Chem.* **2005**, *77*, 7148–7155.
- (81) Schuttlefield, J.; Al-Hosney, H.; Zachariah, A.; Grassian, V. H. *Appl. Spectrosc.* **2007**, *61*, 283–292.
- (82) Hopkins, R. J.; Lewis, K.; Desyaterik, Y.; Wang, Z.; Tivanski, A. V.; Arnott, W. P.; Laskin, A.; Gilles, M. K. *Geophys. Res. Lett.* **2007**, *34*, L18806.
- (83) Desyaterik, Y.; Zaveri, R. A.; Berkowitz, C. M.; Laskin, A.; Hopkins, R. J.; Tivanski, A. V.; Tylliszczak, T.; Gilles, M. K. *J. Geophys. Res., [Atmos.]* **2007**, doi:10.1029/2007JD008954.
- (84) Hand, J. L.; Malm, W. C.; Laskin, A.; Day, D.; Lee, T.; Wang, C.; Carrico, C.; Carrillo, J.; Cowin, J. P.; Collett, J.; Iedema, M. J. *J. Geophys. Res., [Atmos.]* **2005**, *110*, Art. No. D21210.
- (85) Laskin, A.; Wang, H.; Robertson, W. H.; Cowin, J. P.; Ezell, M. J.; Finlayson-Pitts, B. J. *J. Phys. Chem. A* **2006**, *110*, 10619–10627.
- (86) Laskin, A.; Iedema, M. J.; Ichkovich, A.; Graber, E. R.; Taraniuk, I.; Rudich, Y. *Faraday Discuss.* **2005**, *130*, 453–468.



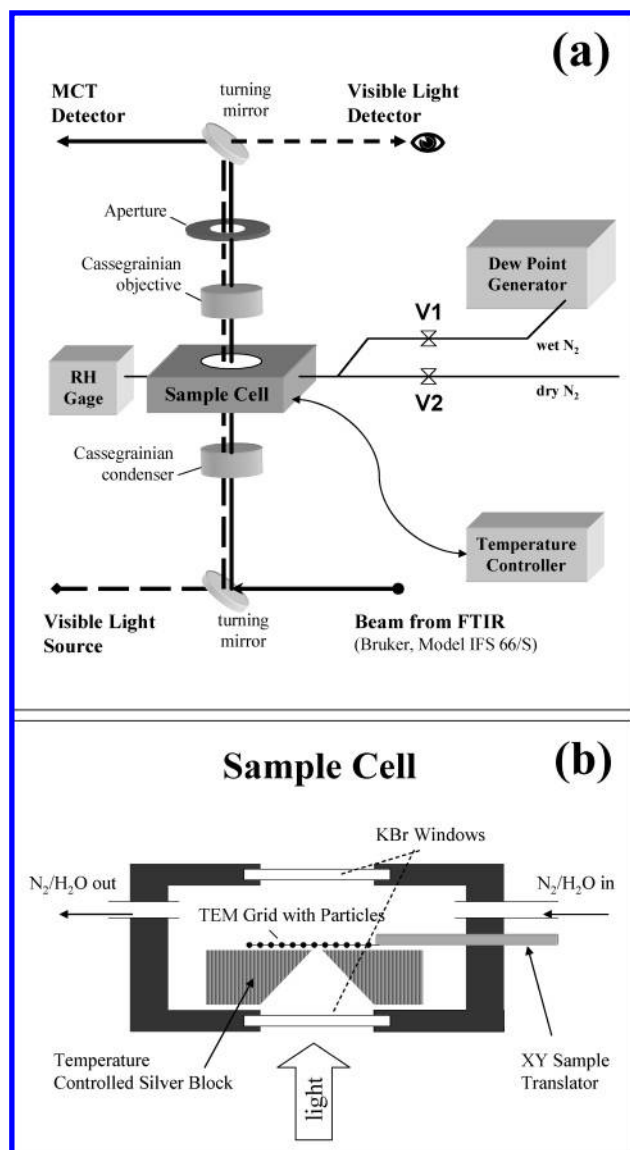


**Figure 1.** Schematics of the micro-FT-IR spectroscopy setup: (a) schematic of the experimental apparatus and (b) side-view schematic of the sample cell.

$\text{cm}^{-1}$  and HOH bending at  $\sim 1640 \text{ cm}^{-1}$ . The integrated absorbance of the OH stretching band from  $3660$  to  $2750 \text{ cm}^{-1}$  is used to calculate the amount of water and water-to-solute molar ratios (WSR). Details of these calculations are discussed later.

Figure 1b shows schematics of the sample cell setup which utilizes a temperature-controlled, environmental stage (model THMS 600, Linkam, Inc.). The filmed grid substrate with particles of interest is held in a sample holder, which is connected to two knobs outside of the stage to provide translation of the holder on the  $x$ - $y$  plane. The holder is fabricated from two thin aluminum sheets that fix the grid tightly in a sandwich-like fashion.<sup>71</sup> The holder itself is tightly affixed to the surface of the temperature-controlled silver block using the standard spring-loaded insert of the Linkam stage. The stage can be sealed once the sample is mounted.

Two KBr windows provide the optical paths for both visible and IR light through the sample cell. Carbon film ( $\sim 50 \text{ nm}$  thickness) of the grid substrates is transparent to visible and IR

light and thus allows the use of the microscope in the transmission mode. The RH over the substrate-deposited particles is controlled by a continuous flow of a mixture of dry and humidified nitrogen. Humidification is provided by a model LI-610 dew point generator (LI-COR, Inc.) with a total flow rate of  $\sim 1.0 \text{ slpm}$ . The RH in the cell can be varied by adjusting the flow rates of the dry and humidified N<sub>2</sub> (see Figure 1a). A dew point hygrometer (model HMP234, Vaisala, Inc.) is used to monitor the RH of the combined flows with an accuracy of  $\pm 1\%$ . After changing the RH to a new setting, a typical delay of 3–5 min is required before stable, reproducible IR spectra can be acquired.

The temperature of the silver block may be controlled with a model TP 93 temperature controller (Linkam, Inc.), though in this particular study the temperature of the sample was kept constant at  $23^\circ\text{C}$ . The sample cell setup presented here is similar to those used to study the microphysics of particles in the research groups of Bertram<sup>33,34,66,67</sup> and Molina.<sup>87–89</sup> This setup enables long exposure time, measurements over statistically significant number of particles (typically  $\sim 100$  particles are monitored in a single experiment), control of the relative humidity, and temperature.

#### Complementary Methods of Single Particle Analyses.

Detailed characterization of environmental particles often requires applications of multiple techniques which are typically interdependent. Often, the information from one method guides subsequent measurements with another method.<sup>71,82–84</sup> Three analytical techniques were applied for additional particle analyses in this work: (a) CCSEM/EDX, for microscopy imaging of particles and speciation of their elemental composition; (b) TOF-SIMS, for depth profiling of sea salt particles; and (c) XRD, for characterization of the phase of  $\text{NaNO}_3$  particles.

An FEG XL30 scanning electron microscope (FEI, Inc.) was used in this work. The microscope is equipped with an X-ray spectrometer (EDAX, Inc) with a Si(Li) detector of an active area of  $30 \text{ mm}^2$  and an ATW2 window. The instrument can also operate in computer-controlled (CCSEM/EDX) mode for analysis of individual particles. Details of this instrument and its applications for the analysis of substrate-deposited particles can be found in a recent review article and references therein.<sup>71</sup>

A TRIFT II time-of-flight secondary ion mass spectrometer (TOF-SIMS) (Physical Electronics, Inc.) was used for depth profiling of sea salt particles. The particles collected on a silicon wafer were placed in the sample holder and subject to a  $^{69}\text{Ga}^+$  source of primary ions in a high-spatial-resolution mode. An accelerating voltage of  $25 \text{ kV}$  was used, and the  $^{69}\text{Ga}^+$  dose rate was  $5.6 \times 10^{17} \text{ ions}\cdot\text{cm}^{-2}$ . A combination of static and dynamic modes of operation allowed depth-profiled speciation of different ions characteristic of the sea salt compounds within individual particles.

The phase of  $\text{NaNO}_3$  particles was identified by a X-ray diffractometer (X'pert, Philips) with an ultrafast X-ray detector. The measurements were carried out with Cu K $\alpha$ 1 radiation at  $45 \text{ kV}$  and  $40 \text{ mA}$ . The scanning was conducted in a continuous mode

(87) Koop, T.; Ng, H. P.; Molina, L. T.; Molina, M. J. *J. Phys. Chem. A* **1998**, *102*, 8924–8931.

(88) Salcedo, D.; Molina, L. T.; Molina, M. J. *Geophys. Res. Lett.* **2000**, *27*, 193–196.

(89) Salcedo, D.; Molina, L. T.; Molina, M. J. *J. Phys. Chem. A* **2001**, *105*, 1433–1439.

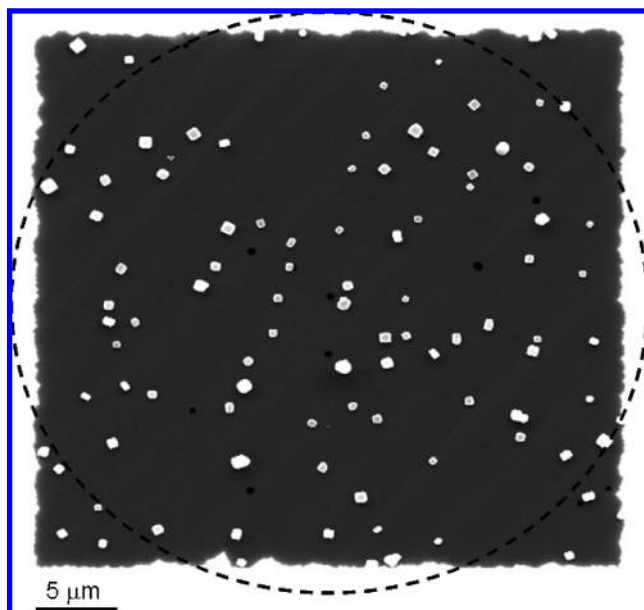


**Figure 2.** SEM image of an ensemble of the NaCl particles deposited in a single  $38 \times 38 \mu\text{m}^2$  cell on the thin film of a grid substrate. Dashed circle indicates the sample area, which is defined by the 0.6 mm aperture over which FT-IR spectra are acquired.

over a  $2\theta$  range from  $20^\circ$  to  $60^\circ$ . In these experiments, samples of  $\text{NaNO}_3$  particles deposited on a  $5 \times 5 \text{ mm}^2$  chip of 1.1.1 silicon wafer were examined. The particle density was  $\sim 5 \times 10^4 \text{ mm}^{-2}$  on the substrate surface.

## RESULTS AND DISCUSSION

**NaCl and Sea Salt Particles.** One notable advantage of the filmed grid substrates is that special marks on the grid can provide a coordinate system that allows locating the same specific area of the sample for the micro-FT-IR and SEM analyses. For instance, Figure 2 shows an SEM image of NaCl particles deposited in a single cell area. The inner area circumscribed by a dashed circle defines an unmasked sample area probed by the IR light. The probed area in Figure 2 is approximately  $1 \times 10^{-9} \text{ m}^2$ , defined by the smallest aperture of  $d = 0.6 \text{ mm}$  in the micro-FT-IR setup. In principle, the probed area can be enlarged by using larger apertures as needed.

Figure 3a shows the FT-IR spectra acquired for an ensemble of NaCl particles over the unmasked sample area at increasing values of RH. The amorphous carbon substrate used in our experiment has a thin layer ( $\sim 30 \text{ nm}$ ) of a Formvar polymer film that enhances the mechanical strength of the substrate. The most intense infrared absorption peaks of Formvar are located near  $1000 \text{ cm}^{-1}$ .<sup>90</sup> In general, they do not overlap with the IR signatures of many atmospheric aerosols. The integrated absorbance of the OH stretching band in the region from  $3660$  to  $2750 \text{ cm}^{-1}$  is used to quantify the amount of water in particles assuming the integrated cross section of  $\bar{\sigma}(\text{OH}) = 1.07 \times 10^{-16} \text{ cm molecule}^{-1}$  reported for bulk water.<sup>91</sup> As can be seen, no appreciable water feature is found near  $3400 \text{ cm}^{-1}$  below  $\text{RH} = 20\%$ . As the RH is incrementally raised, absorption spectra were continuously recorded (spectra

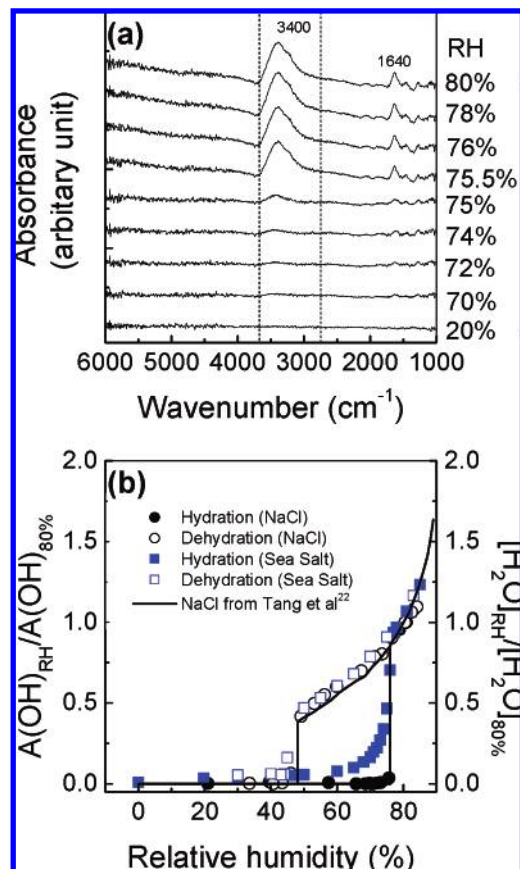


**Figure 3.** (a) FT-IR spectra of NaCl particles undergoing hydration. Spectra are vertically offset for clarity. (b) Hydration/dehydration cycles of NaCl and sea salt particles defined by the integrated areas of the  $\nu(\text{H}_2\text{O})$  mode at a specific RH relative to that at 80% RH (the left axis). Data of Tang et al.<sup>22</sup> are included for comparison (the right axis).

from 20 to 70% RH not shown here). Condensed-phase water remains undetectable until RH around 70% at which point the infrared feature of the water band begins to appear in the spectrum. As RH further increases, a considerable amount of water is taken up. It is seen that NaCl particles deliquesce at  $\sim 75\%$  RH, resulting in an abrupt increase in the absorbance of around  $\sim 3400$  and  $\sim 1640 \text{ cm}^{-1}$ . The swift change indicates that solid NaCl particles deliquesce nearly spontaneously to form saturated solution droplets. Then, the NaCl deliquesced droplets continue to grow with further increases in RH as indicated by water band growth and expansion. Sloping baselines of the FT-IR spectra recorded at  $>75\%$  RH indicate a discernible increase in Mie scattering by the particles at wavenumbers above  $4000 \text{ cm}^{-1}$ . This result is consistent with the increase in particle size at those humidity levels. Specifically, NaCl droplets at 80% RH have approximately twice the size of the dry particles.<sup>85</sup> Thus the  $\sim 2 \mu\text{m}$  droplets, roughly corresponding to a wavenumber of  $5000 \text{ cm}^{-1}$ , give rise to notable light scattering. Below  $4000 \text{ cm}^{-1}$ , scattering is weak and generally does not affect the absorption characteristics such as peak position and shape.<sup>77</sup>

Infrared spectra of the NaCl droplets recorded in the dehydration cycle (not shown here) are similar to those in Figure 3a. Their variations are merely in the reversed order (not shown here). Upon decrease of RH and evaporation, the NaCl droplets gradually lose their water content and water bands in the FT-IR spectra

(90) *FDM Electronic Handbook*. Fiveash Data Management, Inc., 2007. [www.fdmsspectra.com](http://www.fdmsspectra.com).

(91) Al-Abadleh, H. A.; Grassian, V. H. *Langmuir* **2003**, *19*, 341–347.

shrink accordingly until an abrupt shrinkage in absorbance occurs at about 45–48% ERH.

Figure 3b shows a complete hydration/dehydration cycle of NaCl particles recorded in our micro-FT-IR experiment. Here, the change of particle water content resulting from either condensation or evaporation is expressed as the ratio of OH stretching band areas under a specific RH to that at 80% RH ( $A(\text{OH})_{\text{RH}}/A(\text{OH})_{80\%}$ ). This ratio is plotted as a function of RH. As RH increases, solid NaCl particles show nearly no water content up to ~76% DRH when they take up water spontaneously to form deliquesced droplets. The water content then continues to increase gradually toward higher RH. Upon evaporation, the particles slowly shed their water content as RH decreases down to ~48% ERH where crystallization occurs. Lines in the figure represent the particle molar ratios of  $[\text{H}_2\text{O}]_{\text{RH}}/[\text{H}_2\text{O}]_{80\%}$  inferred from the levitation study of Tang et al.<sup>22</sup> The vertical lines indicate DRH and ERH values reported in the same study. As seen, the hydration/dehydration cycle of NaCl particles recorded in our micro-FT-IR experiment agrees with previously published data<sup>22</sup> very well.

For sea salt particles, our data (Figure 3) is also in close agreement with the results reported by Tang et al.<sup>22</sup> Unlike NaCl particles, the sea salt particles begin to take up water and dissolve at RH as low as 30–40% due to the presence of highly hygroscopic magnesium and potassium salts with low characteristic DRH values. With the increase of RH, these hygroscopic salts deliquesce and then undergo steady hygroscopic growth from ~30% RH until about 75% RH, at which point the remaining NaCl in particles deliquesce to become homogeneous droplets. As RH decreases in the dehydration cycle, sea salt droplets evaporate their water gradually until NaCl crystallization sets in at around 45–48%. Different from the NaCl particles, sea salt particles do not dry out completely. Some residual water was always detected even at 0% RH.<sup>29</sup>

This somewhat complex hydration/dehydration behavior of multicomponent sea salt particles can be understood considering the thermodynamic predictions of the mineral sequences expected for the evaporation of seawater.<sup>92</sup> A group of magnesium and potassium salts ( $\text{MgCl}_2 \cdot 6\text{H}_2\text{O}$ ,  $\text{MgSO}_4 \cdot \text{H}_2\text{O}$ ,  $\text{KMgCl}_3 \cdot 6\text{H}_2\text{O}$ , etc.) always crystallizes last in the sequence during dehydration because of their highest water solubility (solubilities of  $\text{MgCl}_2 \cdot 6\text{H}_2\text{O}$ ,  $\text{MgSO}_4 \cdot \text{H}_2\text{O}$ ,  $\text{KMgCl}_3 \cdot 6\text{H}_2\text{O}$ , and NaCl in 100 cm<sup>3</sup> of water at  $T = 25^\circ\text{C}$  are 167, 71, 65, and 40 g, respectively).<sup>93</sup> These predictions imply an important fact that when sea salt particles dry out they keep NaCl crystals in the core and oust magnesium and potassium salts toward the particle surface, and as such, dry sea salt particles have a multilayered structure with the most soluble magnesium and potassium salts concentrated on the top layer, leading to the hydration response of sea salt particles observed at low RH values. This type of heterogeneous core-shell particle morphology has been reported in a number of studies on particles composed of binary, internally mixed salts with significantly different solubilities, e.g., KCl–NaCl,<sup>94</sup> KCl–

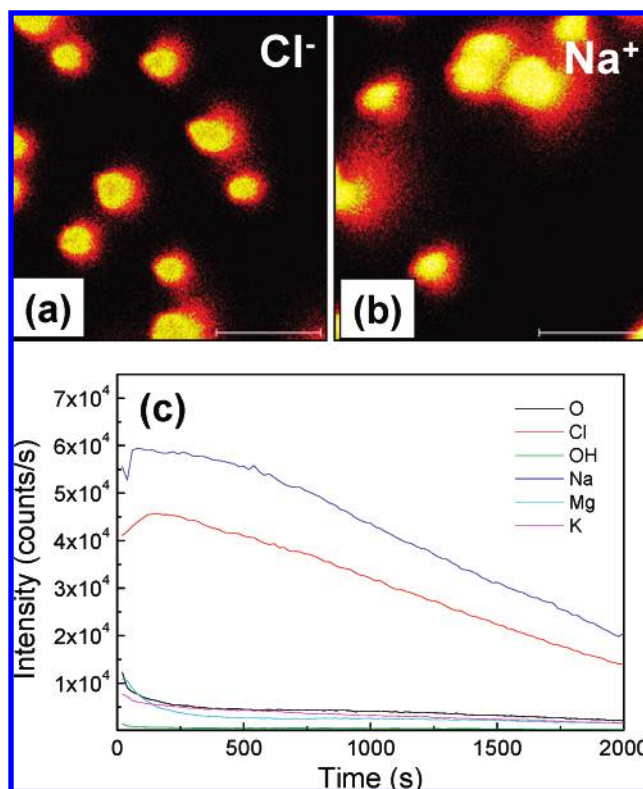


**Figure 4.** TOF-SIMS (a) negative and (b) positive ion maps of sea salt particles probed in the depth-profiling experiment. Maps are 40  $\mu\text{m} \times 40 \mu\text{m}$ . (c) TOF-SIMS peak intensities from region of interest (ROI) analysis for  $\text{Cl}^-$ ,  $\text{O}^-$ ,  $\text{OH}^-$ ,  $\text{Na}^+$ ,  $\text{Mg}^+$ , and  $\text{K}^+$  ions as a function of time. The estimated depth-profiling rate is  $\sim 0.33 \text{ nm/s}$  (see text for details).

$\text{KI}$ ,<sup>94</sup>  $(\text{NH}_4)_2\text{SO}_4$ – $\text{NH}_4\text{NO}_3$ ,<sup>94</sup> and  $\text{NaCl}$ – $\text{NaNO}_3$ .<sup>69,95</sup> However, particles composed of  $\text{NaCl}$ – $\text{NH}_4\text{Cl}$ , two salts of nearly identical solubility, exhibit a homogeneous distribution of both components within the particles.<sup>95</sup> (The solubilities of KCl, KI,  $(\text{NH}_4)_2\text{SO}_4$ ,  $\text{NH}_4\text{NO}_3$ ,  $\text{NaNO}_3$ , and  $\text{NH}_4\text{Cl}$  are 24, 128, 76, 118, 92, and 39 g, respectively, in 100 cm<sup>3</sup> of water at  $T = 25^\circ\text{C}$ ).<sup>93</sup>

To confirm the multilayered structure of dry sea salt particles, we carried out TOF-SIMS analysis on particle samples collected on a silicon wafer chip. Ionic maps (parts a and b) of Figure 4 show the spatial distribution of the  $\text{Cl}^-$  and  $\text{Na}^+$  ion counts recorded over two separate portions of the sample during negative and positive MS modes of the experiment, respectively. The maps indicate the locations of the sea salt particles probed in each of two experiments. Bright colors on the maps indicate more ion counts recorded by the detector. Panel c of Figure 4 shows the  $\text{Cl}^-$ ,  $\text{O}^-$ ,  $\text{OH}^-$ ,  $\text{Na}^+$ ,  $\text{Mg}^+$ , and  $\text{K}^+$  TOF-SIMS signals as a function of depth from the particle surface. As anticipated, the  $\text{Mg}^+$ ,  $\text{K}^+$ ,  $\text{O}^-$ , and  $\text{OH}^-$  ion signals decrease rapidly at the beginning of the depth profiling, whereas the  $\text{Na}^+$  and  $\text{Cl}^-$  ion signals exhibit a characteristic rise-and-fall behavior over a wide range of the depth-profiling experiment. These profiles of the ionic signals are consistent with the layered structure of dry sea salt particles composing the NaCl core coated with a mixture of  $\text{MgCl}_2 \cdot 6\text{H}_2\text{O}$ ,  $\text{MgSO}_4 \cdot \text{H}_2\text{O}$ , and  $\text{KMgCl}_3 \cdot 6\text{H}_2\text{O}$  salts. On the basis of the half-life time of  $\sim 1500 \text{ s}$  observed for the decay of the  $\text{Cl}^-$  and  $\text{Na}^+$

(92) Harvie, C. E.; Weare, J. H.; Hardie, L. A.; Eugster, H. P. *Science* **1980**, *208*, 498–500.

(93) Lide, D. R. *CRC Handbook of Chemistry and Physics*, 81st ed.; CRC Press: Boca Raton, FL, 2000.

(94) Ge, Z.; Wexler, A. S.; Johnston, M. V. *J. Colloid Interface Sci.* **1996**, *183*, 68–77.

(95) Ziemann, P. J.; McMurry, P. H. *J. Colloid Interface Sci.* **1997**, *193*, 250–258.



**Table 1. Coefficients for Calculations of WSR as a Function of Water Activity  $a_w$  for Solutes Used in This Work<sup>a</sup>**

	$a_0 \times 10^{-2}$	$a_1 \times 10^{-3}$	$a_2 \times 10^{-4}$	$a_3 \times 10^{-4}$	$a_4 \times 10^{-4}$	$a_5 \times 10^{-3}$	original refs
NaCl	-7.573	5.891	-1.818	2.798	-2.143	6.553	Tang et al. <sup>22</sup>
sea salt	-4.376	3.591	-1.163	1.874	-1.498	4.773	Tang et al. <sup>22</sup>
NaNO <sub>3</sub>	-4.730	4.012	-1.337	2.199	-1.785	5.737	Tang and Fung <sup>102</sup>
(NH <sub>4</sub> ) <sub>2</sub> SO <sub>4</sub>	-0.5714	0.577	-0.2221	0.424	-0.3977	1.482	Tang and Munkelwitz <sup>20</sup>

<sup>a</sup> WSR =  $\sum_{i=0}^5 a_i a_w^i$

ion signals and the known  $\sim 1 \mu\text{m}$  size of particles, we estimate a depth-profiling rate of 0.33 nm/s for the conditions of our experiment. Therefore, the thickness of the surface layer of magnesium and potassium salts is approximately 30–40 nm.

The micro-FT-IR and TOF-SIMS observations presented here suggest that in real atmospheric environments unreacted sea salt particles have two major physical forms. At high RH, particles are fully deliquesced and present in the form of microdroplets. At low and intermediate RH, a sea salt particle roughly  $1 \mu\text{m}$  in diameter comprises a core of solid NaCl crystal coated with a  $> 30$  nm film of deliquesced magnesium and potassium salts. This conclusion is consistent with a number of previous observations on the heterogeneous chemistry of sea salt. Specifically, Knudsen cell studies on the uptake of HNO<sub>3</sub> and SO<sub>2</sub> gases into dry synthetic sea salt powders indicated that their kinetics were better described as the uptake into liquid rather than into solid-phase material.<sup>96,97</sup> Also, sea salt particles entrained into the atmosphere can undergo a variety of atmospheric reactions<sup>83,98</sup> which may leave particles enriched in additional highly soluble salts, such as NaNO<sub>3</sub>/Mg(NO<sub>3</sub>)<sub>2</sub> and CH<sub>3</sub>SO<sub>3</sub>Na/(CH<sub>3</sub>SO<sub>3</sub>)<sub>2</sub>Mg. As the particles dry out, these compounds will be also present in the outer layer at high concentrations.<sup>69,83</sup>

Figure 3 demonstrates that relative changes in the particle water content can be accurately quantified from the micro-FT-IR experiments for NaCl and sea salt particles. However, quantitative assessment of the WSRs in those particles cannot be obtained from these experiments alone, because mono-atomic anion salts, such as NaCl, MgCl<sub>2</sub>, and KMGCl<sub>3</sub>, have no infrared absorption bands that can be used to quantify the amount of solute. On the other hand, complementary SEM imaging and analysis can be employed to quantify the amount of solute in the particles. In this case, a specific area of the particle sample is imaged first by SEM and then positioned in the micro-FT-IR instrument as illustrated in Figure 2. Thus, the amount of the solute (mol) probed in the experiment can be estimated as

$$[\text{solute}]_{\text{SEM}} = \frac{\rho_{\text{solute}}}{M_{\text{solute}}} \sum_{i < \text{bu}} \frac{\pi}{6} d_{2\text{D-SEM}, i}^3 \quad (1)$$

where  $d_{2\text{D-SEM}, i}$  is the equivalent circle diameter of particle two-dimensional (2-D) projection areas of  $i$ th particle probed by SEM

and  $\rho_{\text{solute}}$  and  $M_{\text{solute}}$  are mass density and molecular weight of dry solute material, respectively.

The amount of water (mol) in the sample area can be estimated using Beer–Lambert’s law

$$\bar{A}(\text{OH}) = \log_{10}\left(\frac{I_0}{I}\right) = \frac{\bar{\sigma}(\text{OH}) \cdot n_{\text{H}_2\text{O}}}{2.303 S_{\mu\text{-FT-IR}}} \quad (2)$$

where  $\bar{A}(\text{OH})$  is the integrated absorbance ( $3660\text{--}2750 \text{ cm}^{-1}$ ) of the OH band ( $\text{cm}^{-1}$ ) probed by micro-FT-IR;  $I_0$  and  $I$  are the transmitted intensities for the bare substrate film and that with particles deposited, respectively;  $\bar{\sigma}(\text{OH}) = 1.07 \times 10^{-16} \text{ cm} \cdot \text{molecules}^{-1}$  is the integrated cross section of the OH band as discussed before;  $n_{\text{H}_2\text{O}}$  is the number of water molecules in the unmasked sample area; and  $S_{\mu\text{-FT-IR}} \approx 38 \times 38 \mu\text{m}^2$  is the size of the probed area, as indicated in Figure 2. In the denominator of eq 2, the factor of 2.303 is  $\ln(10)$ . Equation 2 can be solved for  $n_{\text{H}_2\text{O}}$ . The amount of water in the probed area ( $[\text{H}_2\text{O}]_{\mu\text{-FT-IR}}$ , mol) can be calculated by

$$[\text{H}_2\text{O}]_{\mu\text{-FT-IR}} = \frac{2.303 \bar{A}(\text{OH}) \times S_{\mu\text{-FT-IR}}}{\bar{\sigma}(\text{OH}) \times N_A} \quad (3)$$

where  $N_A = 6.022 \times 10^{23} \text{ mol}^{-1}$  (Avogadro’s number). Finally, the WSR values can be estimated from the combined SEM and micro-FT-IR data by

$$\text{WSR}_{\mu\text{-FT-IR/SEM}} = \frac{[\text{H}_2\text{O}]_{\mu\text{-FT-IR}}}{[\text{solute}]_{\text{SEM}}} \quad (4)$$

The validity of this approach has been elucidated by comparing the  $\text{WSR}_{\mu\text{-FT-IR/SEM}}$  values determined in our experiments with the corresponding values derived from literature data (see Table 1). These comparisons are shown graphically in Figure 5. The 45° diagonal line represents a complete agreement between two sets of the WSR values. The  $\text{WSR}_{\mu\text{-FT-IR/SEM}}$  value obtained for NaCl is in close agreement with the literature data. For sea salt particles, the  $\text{WSR}_{\mu\text{-FT-IR/SEM}}$  value is about a factor of 2 smaller than the literature data. The reason for the discrepancy is the simplified approach applied for the calculation of particle volume which assumes the equivalent circle diameter and spherical morphology of the particle. Because magnesium and potassium salts in sea salt particles are highly hygroscopic and have very low efflorescence points, sea salt particles leaving the diffusion dryer ( $\sim 30\text{--}35\%$  RH) are not entirely dry. As we discussed above, they have layered structures of solid NaCl cores and deliquesced

(96) Gebel, M. E.; Finlayson-Pitts, B. J.; Ganske, J. A. *Geophys. Res. Lett.* **2000**, *27*, 887–890.

(97) DeHaan, D. O.; Finlayson-Pitts, B. J. *J. Phys. Chem. A* **1997**, *101*, 9993–9999.

(98) Finlayson-Pitts, B. J.; Hemminger, J. C. *J. Phys. Chem. A* **2000**, *104*, 11463–11477.



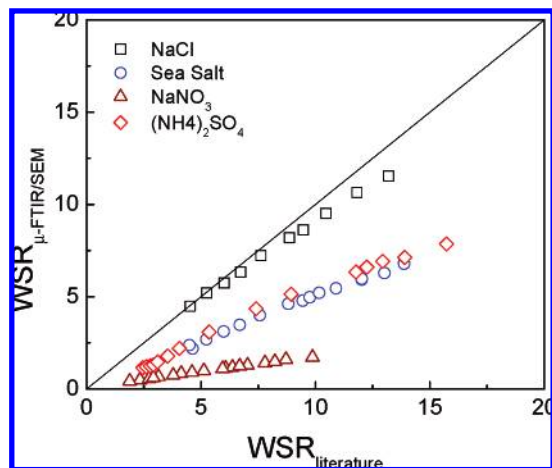


**Figure 5.** WSRs in the samples, determined from integration of water band and 2-D SEM projection areas, compared to those from the literature.<sup>20,22,102</sup>

outer shells. When such particles are impacted onto the substrate, the impactation makes them spread out, resulting in 2-D projection areas larger than those of the original, freely suspended particles, which leads to an overestimation of the amount of solute. Similarly, the  $WSR_{\mu\text{-FT-IR/SEM}}$  values determined for  $(\text{NH}_4)_2\text{SO}_4$  particles also show a similar degree of discrepancy, which again is probably a result of the particle flattening upon impactation. Ammonium sulfate particles have an ERH of  $\sim 33\%$  and were not likely to crystallize at the time of the impactation. For  $\text{NaNO}_3$  particles, however, the  $WSR_{\mu\text{-FT-IR/SEM}}$  values are lower than the literature data by a factor of 5. This observation is consistent with the data to be presented also in the next section that these  $\text{NaNO}_3$  particles were liquid droplets at the time of the impactation, and they were severely shattered against the substrate during sample preparation. As a result they have small vertical relief and their size approximation based on the 2-D projection area leads to greater overestimation of the amount of solute probed in the experiment. Clearly, the combined micro-FT-IR and SEM approach is a useful tool for the quantitative interpretation of the hydration properties of only those particles with morphologies that allow simplified approximation of their volume.

It is important to note that the data of Figure 5 indicate only systematic deviations of the  $WSR_{\mu\text{-FT-IR/SEM}}$  values from the literature data. The nearly linear relationship between the current and literature data for each series of experiments indicates reasonable applicability of the Beer–Lambert law to the conditions of our experiments.

**$\text{NaNO}_3$  Particles.** The hydration behavior of  $\text{NaNO}_3$  particles has been examined using a number of methodologies.<sup>20,26,69,99–102</sup> A majority of these studies have shown that micron- and submicron-size  $\text{NaNO}_3$  particles generated from water solutions exist in metastable, amorphous solid-phase form even at zero relative humidity.<sup>20,26,69,99–101</sup> Those studies reported continuous and reversible growth of the particles without distinct deliquescence

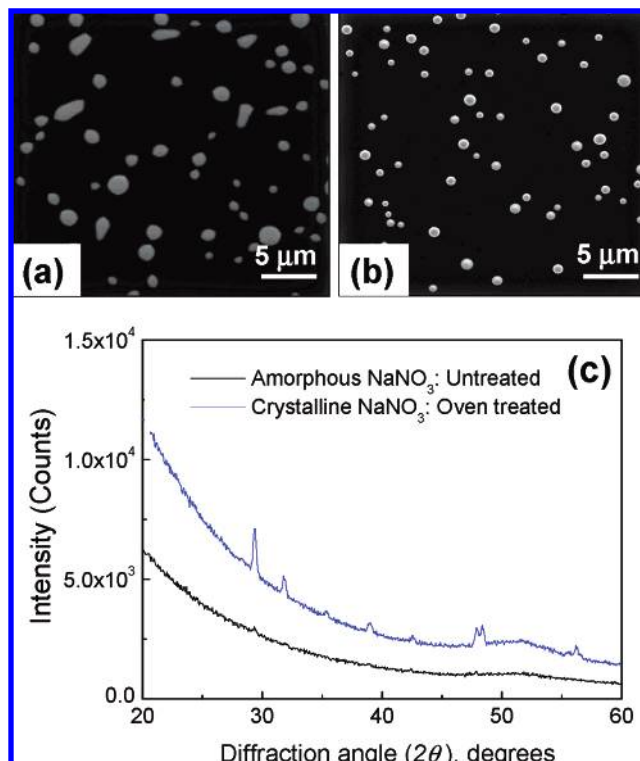


**Figure 6.** SEM images of (a) oven-treated and (b) untreated  $\text{NaNO}_3$  particles. Size bar represents  $10\ \mu\text{m}$ . (c) XRD profiles recorded for oven-treated and untreated  $\text{NaNO}_3$  particles on  $5 \times 5\ \text{mm}^2$  silicon wafers.

and efflorescence points. In contrast, Tang and co-workers<sup>20,102</sup> used a single particle levitation technique and reported a DRH of 74.5% and an ERH in the range from 0.05 to 30% for particles 6 to  $16\ \mu\text{m}$  in diameter. Similar observations were made also by Hoffman et al.<sup>69</sup> in their ESEM experiments with  $\text{NaNO}_3$  particles prepared from crystalline powder.

In order to obtain samples of  $\text{NaNO}_3$  particles comprised of solid crystalline phase, we kept the samples in an oven heated to  $\sim 100\ ^\circ\text{C}$  overnight before their use in experiments. Figure 6 shows SEM images taken for untreated and oven-treated  $\text{NaNO}_3$  particles. The untreated  $\text{NaNO}_3$  particles display a round droplet-like shape even under vacuum condition in the SEM chamber. The morphology of the oven-dried  $\text{NaNO}_3$  particles, however, is somewhat different. The particles are clearly not round-shaped anymore. Though crystalline structure is not evident in the SEM image, substantial crystalline content of  $\text{NaNO}_3$  in these particles can be inferred from the XRD analysis and the corresponding FT-IR spectra taken at low RH. Figure 6c shows an XRD profile recorded for oven-treated and untreated  $\text{NaNO}_3$  particles deposited on silicon wafer chips and dried in the oven side-by-side with those samples prepared on the filmed grid substrates. For comparison, the second XRD profile is also shown for the sample with the untreated particles. As shown, the profile for oven-treated particles shows features indicative of their nitrate crystalline phase, whereas the untreated particles are definitely amorphous.

Figure 7a shows the FT-IR spectra of an ensemble of  $\text{NaNO}_3$  particles during a hydration experiment. At 20% RH, the spectrum consists of a prominent  $\nu_3(\text{NO}_3^-)$  asymmetric stretch band centered at  $1383\ \text{cm}^{-1}$ , with a shoulder at  $1485\ \text{cm}^{-1}$ , which resembles the reported spectra of  $\text{NaNO}_3$  crystalline aerosols.<sup>103</sup>

(99) Gysel, M.; Weingartner, E.; Baltensperger, U. *Environ. Sci. Technol.* **2002**, *36*, 63–68.

(100) Lee, C. T.; Hsu, W. C. *J. Aerosol Sci.* **2000**, *31*, 189–197.

(101) McInnes, L. M.; Quinn, P. K.; Covert, D. S.; Anderson, T. L. *Atmos. Environ.* **1996**, *30*, 869–884.

(102) Tang, I. N.; Fung, K. H. *J. Chem. Phys.* **1997**, *106*, 1653–1660.

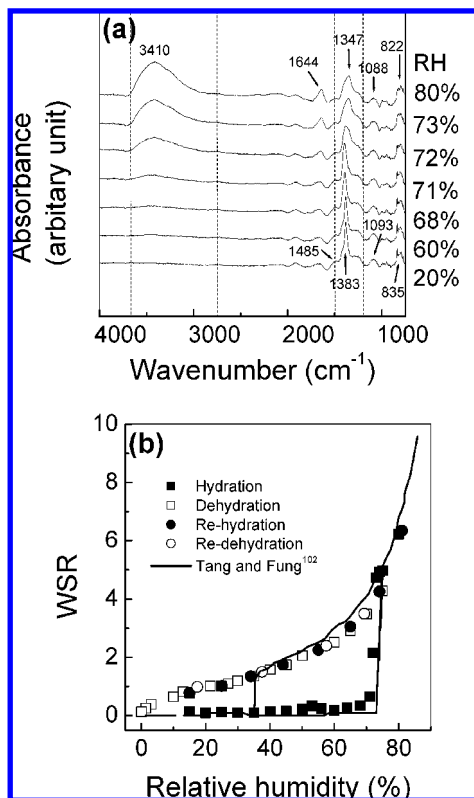


**Figure 7.** (a) FT-IR spectra of oven-treated crystalline  $\text{NaNO}_3$  particles undergoing hydration. Spectra are vertically offset for clarity. (b) Variations of WSRs in  $\text{NaNO}_3$  particles during a two-cycle hydration and dehydration experiment. Data from Tang and Fung<sup>102</sup> are also included for comparison.

The splitting of the degenerate  $\nu_3$  mode is due to a loss of symmetry in the crystal compared with the free ion.<sup>77,104–106</sup> At low RH, particles may form a crystalline solid or highly concentrated aqueous droplets, in which the chemical environment of the nitrate ion is perturbed strongly enough to lower its symmetry from  $D_{3h}$  to  $C_{2v}$ .<sup>106–108</sup> Interactions between water molecules and counter ions may also contribute to the splitting.<sup>110</sup> The  $\nu_3$  doublet has been observed commonly in crystalline nitrate aerosols.<sup>26,103</sup> The narrow band closely resembles previously reported measurements of  $\text{NaNO}_3$  crystalline aerosols.<sup>103</sup> Additionally, the symmetric stretch  $\nu_1(\text{NO}_3^-)$  and the out-of-plane deformation  $\nu_2(\text{NO}_3^-)$  appear at 1093 and 835  $\text{cm}^{-1}$ , respectively. At low RH, no apparent water absorption is found in the infrared spectra of the oven dried particles. When exposed to higher humidities, the infrared spectra show no observable changes until the RH reaches 68–71%, where the absorption of the OH stretch first becomes evident and then rapidly expands at RH higher than 71%. Simultaneously, the narrow 1383  $\text{cm}^{-1}$  band broadens significantly and shifts to  $\sim 1347$

$\text{cm}^{-1}$ . Likewise, the 1093  $\text{cm}^{-1}$  peak has red shifts to 1088  $\text{cm}^{-1}$ . The less-structured broad band observed is characteristic of an aqueous aerosol,<sup>111</sup> and the band shape and position changes are consistent with previous measurements.<sup>26</sup>

To obtain the hygroscopic growth factor for  $\text{NaNO}_3$ , we estimate WSR from the IR spectra by integrating the areas of the  $\nu(\text{H}_2\text{O})$  and  $\nu_3(\text{NO}_3^-)$  bands using the following equation.

$$\text{WSR}_{\mu\text{-FT-IR}} = \frac{n_{\text{H}_2\text{O}}}{n_{\text{NO}_3}} = \frac{\bar{\sigma}(\text{NO}_3^-) \times \bar{A}(\text{OH})}{\bar{A}(\text{NO}_3^-) \times \bar{\sigma}(\text{OH})} \quad (5)$$

where  $n_{\text{H}_2\text{O}}$  and  $n_{\text{NO}_3^-}$  are the numbers of water and the solute molecules, respectively,  $\bar{A}(\text{OH})$  is the integrated (3660–2750  $\text{cm}^{-1}$ ) absorbance of  $\nu(\text{H}_2\text{O})$  band ( $\text{cm}^{-1}$ ), and  $\bar{A}(\text{NO}_3^-)$  is the integrated (1200–1500  $\text{cm}^{-1}$ ) absorbance of  $\nu_3(\text{NO}_3^-)$  band ( $\text{cm}^{-1}$ ). The cross section for  $\text{NO}_3^-$  is  $\bar{\sigma}(\text{NO}_3^-) = 2.5 \times 10^{-16} \text{ cm}^2 \cdot \text{molecule}^{-1}$  determined in an attenuated total reflectance Fourier transform infrared (ATR-FT-IR) experiment using  $\text{NaNO}_3$ /water solutions of known concentrations. The obtained result is in excellent agreement with that reported previously by Al-Abadleh and Grassian<sup>111</sup> ( $2.4 \times 10^{-16} \text{ cm}^2 \cdot \text{molecule}^{-1}$ ) and slightly lower than that reported by Sporleder and Ewing<sup>112</sup> ( $3.0 \times 10^{-16} \text{ cm}^2 \cdot \text{molecule}^{-1}$ ).

Figure 7 shows the variations of  $\text{WSR}_{\mu\text{-FT-IR}}$  in two hydration/dehydration cycles of oven-treated  $\text{NaNO}_3$  particles. During the first cycle, the hydration path exhibits a very sharp deliquescence transition at 71–73% DRH and hygroscopic growth in close agreement with that given by Tang and Fung.<sup>102</sup> However, quite different from that study, the dehydration path does not exhibit the efflorescence transition. As seen, small amounts of water are still present in particles at the end of the first cycle. No efflorescence was observed or could be induced with prolonged experimental time or by repeated hydration/dehydration cycling. Similarly, untreated  $\text{NaNO}_3$  particles showed no phase transitions in repeated hydration/dehydration experiments. These observations indicate that after micron- and submicron-size  $\text{NaNO}_3$  particles were deliquesced, they typically remained either super-saturated liquids or glass solids even under dry conditions. These are consistent with the findings of previous studies.<sup>26,69</sup> Similar hygroscopic behavior was also reported for other nitrate aerosols of atmospheric relevance, including  $\text{NH}_4\text{NO}_3$ ,  $\text{Mg}(\text{NO}_3)_2$ ,<sup>113,114</sup> and  $\text{Ca}(\text{NO}_3)_2$ .<sup>26,102,115</sup>

**$(\text{NH}_4)_2\text{SO}_4$  Particles.** Figure 8a shows the FT-IR spectra of an ensemble of  $(\text{NH}_4)_2\text{SO}_4$  particles in a hydration experiment. At 0% RH, the FT-IR spectrum has a strong absorption band at 1095  $\text{cm}^{-1}$  due to  $\nu_3(\text{SO}_4^{2-})$  asymmetric stretch and highly structured doublets at 3200 and 3040  $\text{cm}^{-1}$  and a sharp peak at 1415  $\text{cm}^{-1}$ , which are assigned to  $\nu_3(\text{NH}_4^+)$  stretch and  $\nu_4(\text{NH}_4^+)$  bending modes, respectively. Their shapes and positions are consistent with previous reports for  $(\text{NH}_4)_2\text{SO}_4$  crystalline aerosol.<sup>27,31,32,57,58,116</sup> During the hydration experiment, condensed-phase

(103) Weis, D. D.; Ewing, G. E. *J. Phys. Chem. A* **1999**, *103*, 4865–4873.

(104) Frost, R. L.; James, D. W. *J. Chem. Soc., Faraday Trans.* **1982**, *78*, 3249–3261.

(105) Frost, R. L.; James, D. W. *J. Chem. Soc., Faraday Trans.* **1982**, *78*, 3223–3234.

(106) Vollmar, P. M. *J. Chem. Phys.* **1963**, *39*, 2236–2248.

(107) Chang, T. G.; Irish, D. E. *J. Phys. Chem.* **1973**, *77*, 52–57.

(108) Irish, D. E.; Walrafen, G. E. *J. Chem. Phys.* **1967**, *46*, 378–384.

(109) Hester, R. E.; Plane, R. A.; Walrafen, G. E. *J. Chem. Phys.* **1963**, *38*, 249–250.

(110) Liu, J. H.; Zhang, Y. H.; Wang, L. Y.; Wei, Z. F. *Spectrochim. Acta, Part A* **2005**, *61*, 893–899.

(111) Al-Abadleh, H. A.; Grassian, V. H. *J. Phys. Chem. B* **2003**, *107*, 10829–10839.

(112) Sporleder, D.; Ewing, G. E. *J. Phys. Chem. A* **2001**, *105*, 1838–1846.

(113) Zhang, Y. H.; Choi, M. Y.; Chan, C. K. *J. Phys. Chem. A* **2004**, *108*, 1712–1718.

(114) Ha, Z. Y.; Chan, C. K. *Aerosol Sci. Technol.* **1999**, *31*, 154–169.

(115) Lightstone, J. M.; Onasch, T. B.; Imre, D.; Oatis, S. J. *Phys. Chem. A* **2000**, *104*, 9337–9346.

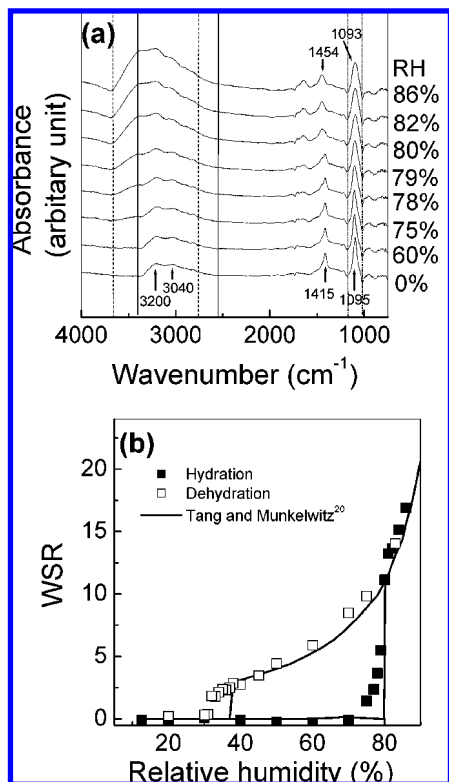


**Figure 8.** (a) FT-IR spectra of crystalline  $(\text{NH}_4)_2\text{SO}_4$  particles undergoing hydration. Spectra are vertically offset for clarity. (b) WSRs in  $(\text{NH}_4)_2\text{SO}_4$  particles during a single-cycle hydration/dehydration experiment. Data from Tang and Munkelwitz<sup>20</sup> are also included for comparison.

water starts to appear at  $\sim 75\%$  RH. As the  $(\text{NH}_4)_2\text{SO}_4$  particles are transformed into liquid droplets and despite the broad water envelope, the  $\text{NH}_4^+$  stretch mode is still clearly resolved. A slight broadening and red shifts are observed for the  $\nu_3(\text{SO}_4^{2-})$  and the  $\nu_4(\text{NH}_4^+)$  absorption bands as RH increases. The amount of solute was estimated using the integrated  $(1020\text{--}1180\text{ cm}^{-1})$  absorbance of the  $\nu_3(\text{SO}_4^{2-})$  band ( $\bar{A}(\text{SO}_4^{2-}), \text{cm}^{-1}$ ) and integrated cross section  $\bar{\sigma}(\text{SO}_4^{2-}) = 2.0 \times 10^{-16} \text{ cm}^2 \text{ molecule}^{-1}$  of sulfate measured from ATR-FT-IR experiments using  $(\text{NH}_4)_2\text{SO}_4$  solutions of known concentrations. The obtained integrated cross section is consistent with the literature value reported by Weis and Ewing<sup>116</sup> of  $\bar{\sigma}(\text{SO}_4^{2-}) = 2.2 \times 10^{-16}$  near  $1120\text{ cm}^{-1}$ . The integrated absorbance of the  $\nu_3(\text{NH}_4^+)$  stretch at  $2550\text{--}3400\text{ cm}^{-1}$  measured at  $0\%$  RH was used to subtract the  $\text{NH}_4^+$  contribution from the overlapping  $\nu(\text{H}_2\text{O})$  water bands. Figure 8b shows the hydration/dehydration cycles determined for  $(\text{NH}_4)_2\text{SO}_4$  particles. For comparison, the literature data of Tang and Munkelwitz<sup>20</sup> are also included in the figure. In this case, a hysteresis cycle is observed with respect to water condensation and evaporation, indicating abrupt deliquescence and efflorescence transitions at  $75\%$  DRH and  $33\%$  ERH, respectively.

(116) Weis, D. D.; Ewing, G. E. *J. Geophys. Res., [Atmos.]* **1996**, *101*, 18709–18720.

(117) Gao, Y.; Chen, S. B.; Yu, L. E. *J. Phys. Chem. A* **2006**, *110*, 7602–7608 and references therein.

These results are again in good agreement with previous studies<sup>117</sup> that reported values of DRH =  $79\text{--}80\%$  and ERH =  $32\text{--}35\%$  characteristic of submicron  $(\text{NH}_4)_2\text{SO}_4$  particles.

## CONCLUDING REMARKS

In this work, a novel micro-FT-IR approach was presented for studying hygroscopic behaviors of aerosols. Through the case studies, we have showed that when supplemented by several complementary instrumentation techniques, the micro-FT-IR approach could provide insightful, quantitative data on aerosol hydration and dehydration. In conjunction with field sampling devices, the approach is a promising technique for studies of aerosols collected in field campaigns where the ability to deploy other techniques is limited.

To obtain reliable data on the hygroscopic properties for aerosols, several cautionary issues must be carefully dealt with. In general, integrated cross sections can be measured accurately with no more than  $20\%$  deviation. On the other hand, the uncertainty from absorbance integration could be as large as  $30\text{--}40\%$  owing to different integration options and baseline correction. These uncertainties could be reduced with better signal-to-noise ratios. In addition, the use of consistent integration and baseline correction methods throughout the absorbance and cross section measurements can lead to the cancellation of systematic deviations. A reasonably large amount of particles in the probed field of view is usually preferred, even though the micro-FT-IR technique can detect water content as low as  $1\text{ pmol}$ , according to our case study with NaCl particles. One simply way to include a greater number of particles in the probed area is to increase the aperture size. However, this approach could introduce a fringe effect stemming from IR reflection in the thin carbon film and Cu grid. The use of TEM grids with coarse mesh (large cell area) or other substrates such as diamond or silicon nitrate film may help remove this complication.

## ACKNOWLEDGMENT

The work was supported by Tropospheric Chemistry and Radiation Sciences programs at the National Aeronautics and Space Administration (Grant Nos. NNG06GE89G and 796 NNG06GI51G) and the Atmospheric Science Program of the Department of Energy's Office of Biological and Environmental Research (DOE OBER). This research was performed in the Environmental Molecular Sciences Laboratory (EMSL), a national scientific user facility sponsored by the Department of Energy's Office of Biological and Environmental Research (DOE OBER) and located at Pacific Northwest National Laboratory (PNNL). PNNL is operated by the U.S. Department of Energy by Battelle Memorial Institute under contract No. DE-AC06-76RL0 1830. Z.Y. acknowledges sponsorship provided by the 2004 Summer Research Institute on Interfacial and Condensed Phase Chemical Physics organized at PNNL.

Received for review August 2, 2007. Accepted November 8, 2007.

AC701638R